

<https://doi.org/10.1038/s41529-026-00767-y>

Effect of iron and manganese on the corrosion resistance of contaminated secondary Al-Si-Mg cast alloys

Check for updates

Qiqi Li¹ ✉, Eugen Gazenbiller¹, Lukas Cäsar Jarren¹, Mikhail L. Zheludkevich^{1,2} & Daniel Höche¹

It is well established that micro-galvanic corrosion induced by impurity phases during metallurgical processing limits the application of recycled aluminum. This study investigates the corrosion behavior of AlSi₇Mg_{0.3} alloy with two varying Mn/Fe ratios. A combined approach involving electrochemical testing, salt spray exposure, and finite element modeling was employed to clarify the roles of Fe-rich and Mn-rich intermetallic phases in corrosion progression. The appropriate addition of Fe and Mn promoted the formation of “Chinese-script” α -Al(FeMn)Si phases and improved alloy corrosion resistance by refining the dendritic structure and lowering galvanic activity. Accelerated exposure experiments revealed that the β -AlFeSi phase exhibited strong cathodic activity and facilitated phase-selective dissolution adjacent to the α -Al matrix. In contrast, the Chinese-script α -Al(FeMn)Si phase presented partial dissolution at peripheries, marking the initiation of localized attack. However, the phase is electrochemically inert and retains the original morphology, which has little effect on the corrosion propagation by reducing micro-galvanic coupling with the matrix. Complementary to a finite element corrosion model successfully captured the selective dissolution of the Al-Si and predicted the transient corrosion front progression as found in experiments. The integrated approach applied in this work offers theoretical guidance for corrosion-related impurity assessment of recycled aluminum alloys.

Aluminum alloys are widely recognized as lightweight construction materials promoting fuel efficiency, reducing energy consumption, providing a good weight-to-strength ratio, and lowering CO₂ emissions due to their low density^{1–4}. In particular, Al-Si-Mg cast alloys are extensively used in automotive structures and engine components for their superior castability, mechanical strength, and corrosion resistance^{5–7}. Additionally, aluminum offers excellent recyclability, with secondary production consuming only 5–10% of the energy required for primary aluminum⁸. This makes recycled aluminum a sustainable and cost-effective material for industrial applications, especially in transportation.

However, the widespread application of recycled aluminum is hindered by metallurgical challenges. Elements such as Fe, Mn, Cu, and Mg are difficult to eliminate during remelting due to the variability and complexity of scrap sources^{9–12}. These elements tend to form intermetallic particles (IMPs) like α -Al(FeMn)Si, β -AlFeSi, π -AlFeSiMg, Q-AlCuMgSi^{13–15}. The formation and morphology of these IMPs negatively affect the corrosion and mechanical performance of aluminum alloys^{14–17}. For example, in corrosive environments, Fe-rich IMPs act as cathodes, accelerating localized

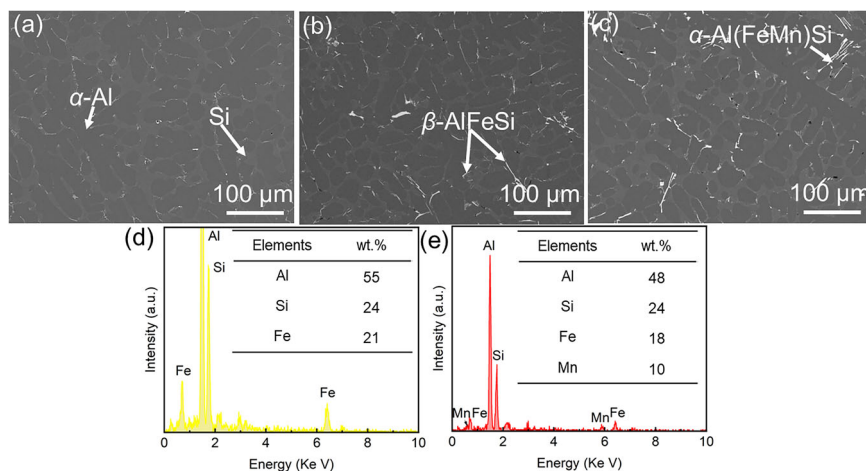
corrosion, such as pitting, intergranular corrosion (IGC), and filiform corrosion^{14,18,19}.

Among various IMPs, the plate-like β -AlFeSi phase is particularly detrimental due to its strong cathodic character, exhibiting a volta potential difference of approximately 200 mV relative to the surrounding Al matrix^{20,21}. This pronounced potential difference significantly promotes micro-galvanic coupling with the aluminum matrix²². Increasing the Mn/Fe ratio is a well-established strategy to suppress the formation of the deleterious phase^{18,21,23}. Mn promotes the formation of more stable α -Al(FeMn)Si phases instead of β -AlFeSi. The phase is less electrochemically active, thereby enhancing both the corrosion resistance and mechanical performance of the alloy^{24–28}. For instance, an Mn/Fe ratio close to 1.3 has been reported to maximize ductility²⁹. With the addition of 0.07 or 0.13 Mn, the plate-like β -AlFeSi in A356 is replaced by the rod-like α -Al(Mn, Fe)Si³⁰. Thermodynamic analyses further indicate that when Fe concentration reaches 4.19 wt%, α -Al(FeMn)Si becomes the dominant precipitate phase³¹. Despite extensive investigations that have predominantly addressed short-term

¹Institute of Surface Science, Helmholtz-Zentrum Hereon, Geesthacht, Germany. ²Institute for Materials Science, Kiel University (CAU), Kiel, Germany.

✉ e-mail: qiqi.li@hereon.de

Fig. 1 | SEM images of as-cast alloys and EDS spectra of plate-like particle and Chinese-script particle. **a–c** SEM images showing the typical surface morphologies of alloys A, B, and C, respectively. Distinct regions with different contrasts correspond to the α -Al matrix, eutectic Si, and intermetallic particles distributed throughout the microstructure. The eutectic Si phase is indicated by white arrows. **d** Representative EDS spectrum of a plate-like β -AlFeSi intermetallic particle. **e** Representative EDS spectrum of a Chinese-script α -Al(FeMn)Si particle, confirming their elemental compositions. SEM scanning electron microscopy, EDS energy-dispersive spectroscopy.



corrosion behavior, the long-term stability of aluminum alloys containing a higher level of contamination by impurity elements and their associated corrosion processes remains inadequately understood.

Previous studies have provided a theoretical basis for revealing the role of impurity phases in corrosion initiation and propagation. For example, Peng³² et al. investigated the electrochemical corrosion behavior of Al-Zn-Mg-Cu alloys and pointed out that the influence of impurity phases on localized corrosion is crucial. Gao²³ and Kayani²¹ et al. found that the corrosion of Al-Si-Mg alloys often starts from IMPs, while Kim¹⁸ et al. further suggested that optimizing the morphology of IMPs can help improve the corrosion resistance. Simulation studies using finite element methods (FEM) have modeled current and potential distributions to predict corrosion tendencies^{32,33}. However, conventional FEM approaches have limitations in the evolution of micro-secondary phases with heterogeneous structures and in capturing evolving corrosion interfaces under thin electrolyte film exposure.

In response to these limitations, this study investigates starting from a high Fe impurity (0.55 wt%), which is sufficient to promote the formation of plate-like β -AlFeSi. This approach ensures the industrial relevance and enables a realistic assessment of corrosion under contamination, Fe levels of secondary aluminum. Furthermore, this work examines Mn-modified efficiency within a specific Mn/Fe ratio range. By correlating microstructural evolution with both immersion and thin-film (salt-spray) corrosion behavior, the study identifies and experimentally validates a critical Mn/Fe effectiveness window (0.3–0.6). This offers a practical guideline for the control of Mn additions in the industrial melt process. This compositional variation enables a detailed evaluation of phase-specific electrochemical responses and their influence on corrosion behaviors. A combined experimental and numerical approach is adopted to clarify the underlying corrosion mechanisms. Dedicated salt spray tests emulating thin-film electrolyte conditions were conducted to monitor the corrosion morphology evolution of Fe-rich and Mn-rich intermetallic phases. In particular, the electrochemical characteristics and corrosion progression associated with different IMPs in impurified Al-Si-Mg alloys are explored. In parallel, a computational FEM approach is employed to simulate the evolution of the corrosion front in a two-phase system, allowing physically consistent tracking of dynamic boundary movement. The model incorporates the experimentally measured polarization behavior of the intermetallic phases, together with their volume fractions and spatial distributions, enabling accurate simulation of the progressing corrosion interface. By integrating thin film corrosion testing with advanced modeling techniques, this work provides new insights into the degradation mechanisms of the contaminated secondary aluminum alloys induced by impurity phases related to salt spray corrosion.

Results

Microstructure characterization

Backscattered SEM images of the as-cast Al-Si-Mg alloys (Fig. 1a–c) displayed three distinct regions with different contrast levels. Complementary EDS results in Fig. 1d and e confirmed the presence of intermetallic particles β -AlFeSi and α -Al(FeMn)Si.

In alloy A, the microstructure was predominantly composed of α -Al dendrites, characterized by a secondary dendrite arm spacing (SDAS) of $(21 \pm 7) \mu\text{m}$ with the line-intercept method. The eutectic Al-Si region formed a continuous network-like morphology, with an average equivalent circle diameter (ECD) of $(17 \pm 6) \mu\text{m}$. A limited number of β -AlFeSi intermetallics were observed along the eutectic boundaries. This observation aligns with the low Fe content of alloy A, which restricts the formation of Fe-rich intermetallic phases.

In contrast, alloy B contains a higher Fe concentration, resulting in a pronounced increase in the formation of plate-like β -AlFeSi. The α -Al matrix exhibited a reduced SDAS of $(16 \pm 4) \mu\text{m}$, and the eutectic Si clusters displayed an ECD of $(12 \pm 4) \mu\text{m}$. As shown in Fig. 1b, the Fe-rich phase appeared as elongated or plate-like structures with a maximum length of approximately $51 \mu\text{m}$ and widths of $1.5 \mu\text{m}$ to $3.2 \mu\text{m}$.

In alloy C, the SDAS measured $(17 \pm 4) \mu\text{m}$, while the eutectic Si clusters exhibited an ECD of $(11 \pm 5) \mu\text{m}$. The increased Mn/Fe ratio effectively suppressed the formation of plate-like β -AlFeSi phases^{34,35}. Instead, Chinese-script α -Al(FeMn)Si intermetallics were observed, with EDC ranging from $24.2 \mu\text{m}$ to $74.3 \mu\text{m}$, as shown in Fig. 1c. Compared with alloy A, the SDAS decreased by 7% to 25%, while the size of eutectic Si was reduced by 30% to 45%.

Corrosion behavior of contaminated Al-Si-Mg alloys in NaCl solution

The EIS results for the three alloys in a 3.5 wt% NaCl solution over a frequency range of 10^5 Hz to 10^{-2} Hz are shown in Fig. 2. At low frequencies, the maximum $|Z|$ of the three alloys at 0.01 Hz was observed after 5 h, followed by a decrease at 12 h. All alloys exhibited a gradual evolution of impedance with no statistically significant differences when considering the standard deviation in Table 1. Bode plots reveal at least two distinct relaxation processes. The first relaxation process appears in the middle-frequency range, corresponding to the capacitive behavior of the native oxide layer on the surface of aluminum alloy. The second process, located in the low-frequency range, is associated with the electrochemical activity at the newly exposed surface.

The EECs used to fit the EIS data are illustrated in Fig. 2d and e. Circuit components are defined as follows: R_s denotes the resistance of bulk solution, R_f represents the resistance of surface layer, R_{ct} signifies charge transfer resistance. Q_f represents the CPE of passive film, Q_{dl} signifies the CPE of double layer. A comparison of the EIS fitting results using the EECs in

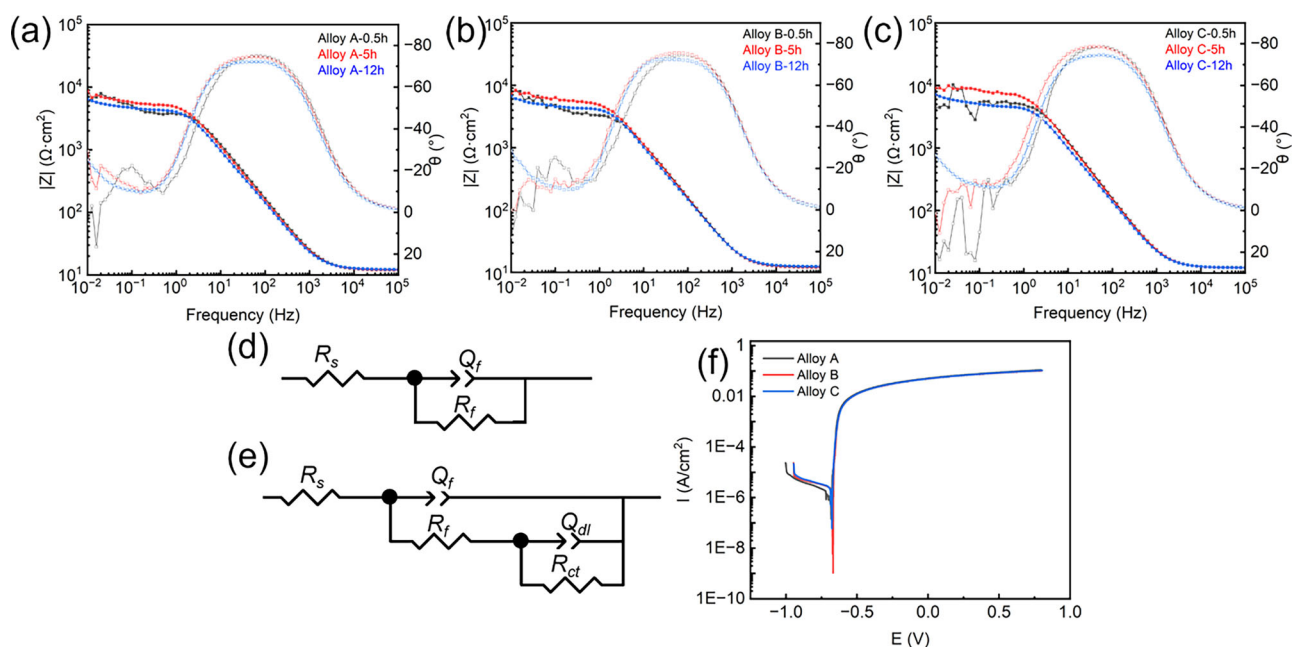


Fig. 2 | Electrochemical performance and Equivalent electrical circuits modeling of three Al-Si-Mg alloys. a–c Bode plots of alloys A, B, and C measured after 0.5, 5, and 12 h immersion over a frequency range from 100 kHz to 0.01 Hz. Black, red, and blue curves represent 0.5, 5, and 12 h exposure, respectively. d, e Equivalent electrical

circuits used to fit the impedance spectra. R_s denotes solution resistance, R_f surface film resistance, R_{ct} charge-transfer resistance, Q_f the constant phase element (CPE) of the passive film, and Q_{dl} the double-layer CPE. f Potentiodynamic polarization curves of alloys A, B, and C. EIS, electrochemical impedance spectroscopy.

Table 1 | Equivalent electrical circuit fitting parameters of EIS results for the three aluminum alloys in 3.5 wt% NaCl solution

Materials	$Q_f(\Omega^{-1} \cdot \text{cm}^{-2} \cdot \text{s}^n)$	n_f	$R_f(\text{k}\Omega \cdot \text{cm}^2)$	$Q_{dl}(\Omega^{-1} \cdot \text{cm}^{-2} \cdot \text{s}^n)$	n_{dl}	$R_{ct}(\text{k}\Omega \cdot \text{cm}^{-2})$
Alloy A-0.5h	$(1.76 \pm 0.78) \times 10^{-5}$	0.91 ± 0.11	4.4 ± 1.4			
Alloy A-5h	$(2.04 \pm 0.88) \times 10^{-5}$	0.90 ± 0.12	5.9 ± 1.1			
Alloy A-12h	$(2.39 \pm 0.76) \times 10^{-5}$	0.89 ± 0.12	4.7 ± 0.9	$(3.74 \pm 0.64) \times 10^{-3}$	0.90 ± 0.14	5.1 ± 0.7
Alloy B-0.5h	$(1.88 \pm 0.91) \times 10^{-5}$	0.90 ± 0.11	3.7 ± 1.1			
Alloy B-5h	$(1.98 \pm 0.85) \times 10^{-5}$	0.90 ± 0.11	5.9 ± 1.2			
Alloy B-12h	$(2.12 \pm 0.51) \times 10^{-5}$	0.90 ± 0.11	4.3 ± 0.7	$(2.62 \pm 0.64) \times 10^{-3}$	0.89 ± 0.13	5.3 ± 1.4
Alloy C-0.5h	$(1.62 \pm 0.74) \times 10^{-5}$	0.93 ± 0.11	5.8 ± 1.4			
Alloy C-5h	$(1.72 \pm 0.65) \times 10^{-5}$	0.92 ± 0.11	8.3 ± 2.1			
Alloy C-12h	$(2.09 \pm 0.74) \times 10^{-5}$	0.91 ± 0.12	4.5 ± 0.9	$(2.21 \pm 0.65) \times 10^{-3}$	0.89 ± 0.13	6.2 ± 1.1

Fig. 2d and e is provided in Table 1. The time-dependent evolution of impedance responses reflects the dynamic balance between surface oxide film stability and interfacial electrochemical activity. SEM and EDS images in Fig. 3a–c show that the eutectic Al-Si phase suffered the mainly corrosion attack. Furthermore, the surface morphologies observed in Fig. 3d–f after impedance testing indicate a relatively lower density of corrosion pits on the Mn-rich alloy C. However, deeper pitting was still present in certain localized areas, while other regions remained. This heterogeneous corrosion behavior may be related to the refined microstructure of alloy C, in which the formation of plate-like β -AlFeSi is suppressed and Chinese-script α -Al(FeMn)Si phases are promoted.

In addition to impedance analysis, potentiodynamic polarization tests were conducted to further evaluate the phase-selective corrosion susceptibility of the Al-Si-Mg alloys. The polarization curves are shown in Fig. 2f. Among the three alloys, the anodic current density increases rapidly for all three alloys, indicating that the oxide film on the aluminum alloy surface is prone to breakdown. Meanwhile, the similar shapes of the polarization curves suggest that the alloys display comparable electrochemical behavior in the polarization test.

The penetration depths obtained from low-magnification SEM images (Fig. 4a–c) were 42 μm , 53 μm , and 47 μm for alloys A, B, and C,

respectively. Cross-sectional SEM images (Fig. 4d–f) show that corrosion preferentially initiated near the IMPs and α -Al matrix regions in alloys B and C (red arrows). And the eutectic Al-Si phase promoted more extensive attack in all three alloys due to the netshape-like structure. This corrosion morphology indicates that the attack propagated along the eutectic Al-Si matrix, consistent with intergranular corrosion of the three alloys. Fe/Mn-rich intermetallic particles induced trenching, and the associated local potential gradients likely facilitated electrolyte ingress along IMP boundaries.

Corrosion morphology after salt spray test

Traditional electrochemical techniques, such as polarization and EIS, rely on bulk electrolytes and predominantly reflect the averaged behavior of the entire exposed surface. However, atmospheric corrosion occurs under micrometer-scale electrolyte films where anodic and cathodic sites can become highly localized and strongly influenced by local chemical condition^{36,37}. Factors like enhanced oxygen diffusion, uneven electrolyte film distribution, and local chemical microenvironments play key roles in real degradation^{16,36}. To better replicate real conditions of the casting alloys-based component, this study employed salt spray testing to reveal in thin electrolyte condition corrosion of three aluminum alloys as well. Figure 5

Fig. 3 | Surface morphologies with corresponding EDS spectra of alloys A, B, and C after 12 h of EIS testing in 3.5% NaCl. a–c SEM images and corresponding EDS elemental mappings of alloys A, B, and C after 12 hours of EIS exposure. Aluminum, silicon, iron, and manganese are shown as green, blue, yellow, and orange distributions, respectively, revealing preferential corrosion around intermetallic particles. d–f Three-dimensional surface profiles illustrating localized dissolution depths for the three alloys.

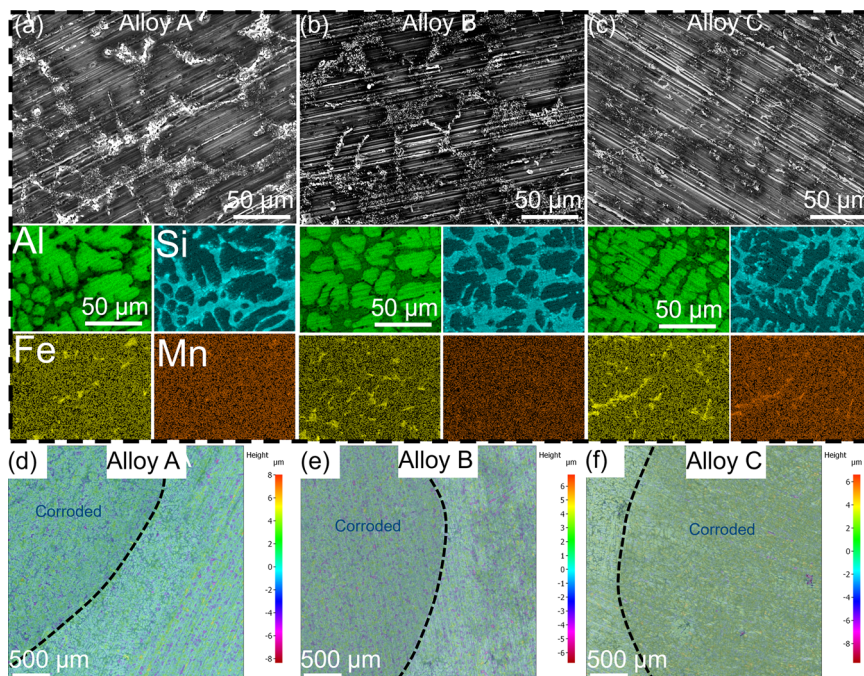
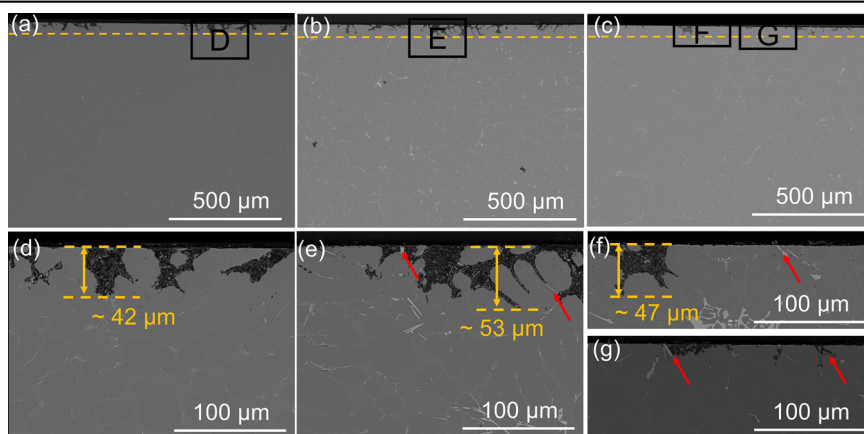


Fig. 4 | SEM images of alloy A, alloy B, and alloy C after potentiodynamic polarization test. a–c Low-magnification SEM images showing penetration depths of approximately 42 μm , 53 μm , and 47 μm for alloys A, B, and C, respectively. The orange dashed line is parallel to the maximum depth of corrosion and the sample surface. d–f Higher-magnification images revealing that corrosion preferentially initiates near intermetallic particles and adjacent α -Al matrix regions, as indicated by red arrows.



shows the surface morphologies of the three alloys after 72, 157, and 230 h of exposure. Uniform dark corrosion products were visually observed during early stages (72–157 h), suggesting a relatively stable progression of corrosion on alloy A. At 230 h, yellow and colorless deposits appeared, aligned with droplet trails, indicating localized dissolution processes. SEM cross-sections (Fig. 6a–c) revealed shallow corrosion depth, with preferential attacks occurring at the eutectic Al–Si phases adjacent to α -Al matrix.

In contrast, alloy B demonstrated more aggressive corrosion from the beginning. After 72 h, the surface showed colorless corrosion products and dark trails of droplets. At 230 h, the accumulation of dark corrosion products was observed over large surface areas. This accelerated degradation was mainly attributed to the presence of the β -AlFeSi phase, which acted as a strong cathodic site and promoted galvanic dissolution of the surrounding Al matrix. SEM and EDS analysis confirmed the β -AlFeSi phase (yellow arrows), leading to trenching in active electrochemical corrosion areas as mentioned earlier. Some oxidation products (yellow circles) were formed, corresponding to the pitting holes on the surface. The same result was also observed in Fig. 6j on alloy B after 72 hours.

Although alloy C contained similar Fe content to alloy B, its corrosion behavior differed significantly. Optical images after prolonged exposure

visually observed the formation of reddish-brown corrosion products, while dark trails were less pronounced. SEM micrographs Fig. 6f and i showed that the α -Al(FeMn)Si intermetallics remained partly intact (red arrows), with significantly less fragmentation or detachment. It should be noted that the reddish-brown appearance mainly results from the accumulation of corrosion products on the surface, rather than the extensive dissolution of intermetallic particles. Nevertheless, as shown in the magnified images in Fig. 6k and l, some partial dissolution may still occur at the α -Al(FeMn)Si particle periphery during localized corrosion. Consequently, trenching developed around the phase, and some stable location corrosion was able to propagate into the surrounding matrix. Although the Mn-containing phase can locally promote stable localized corrosion at its periphery, it exerts little influence on the overall propagation of corrosion in the surrounding Al-matrix. Therefore, the Mn-rich IMPs remained largely intact, showing only limited trenching features.

Microgalvanic corrosion simulation of alloy A

The electrolyte current density distribution and micro-galvanic corrosion behavior of alloy A in a thin film NaCl solution were investigated using a finite element model, as shown in Fig. 7. In this model, the electrolyte was simplified as a homogeneous medium with a constant Cl^- concentration

and initial neutral pH. Although dynamic variations in the electrolyte environment under salt spray conditions were not included, the simulation reproduced key features observed experimentally for alloy A. The simulation results reveal that charge transfer is driven by the potential difference between the eutectic Al-Si regions and the surrounding α -Al matrix, leading to localized anodic dissolution of the Al-Si. Corrosion propagates along the interconnected eutectic network, confirming the galvanic coupling between the α -Al and the secondary phase. The simulated electric current density

field exhibits pronounced spatial inhomogeneity. Higher current densities are concentrated near the corrosion front, and coarser impurity particles tend to generate stronger local currents, likely due to their increased electrochemical surface area and more continuous electron conduction paths.

The model also captures the progressive deepening of the corrosion front, as shown in Fig. 7d–f, which is consistent with both experimental morphologies and previous findings³⁸. After virtual 365 hours of simulated immersion (Fig. 8), current density vector fields indicate selective dissolution of the eutectic Al-Si phase, while the α -Al matrix remains nearly unaffected, with current densities approaching nearly zero. The resulting corrosion morphology is of a known characteristic of intergranular attack. The simulation can also be extended to study the effect of impurities on corrosion, particularly their role within heterogeneous microstructure during initial corrosion for further model development.

Discussion

Based on the above experiments, the corrosion behavior of three alloys is governed by the distribution, morphology, and electrochemical activity of impurity particles. Owing to their pronounced cathodic behavior^{14,21}, Fe/Mn-containing IMPs readily form micro-galvanic couples with adjacent α -Al. Furthermore, the plate-like morphology increases the interacting interfacial area with the surrounding α -Al matrix, intensifying local galvanic coupling and promoting even more localized corrosion. Additionally, the optimization of eutectic SDAS affects the characteristic path of corrosion penetration, thereby influencing the extent and morphology of corrosion propagation. The observation that the α -Al(FeMn)Si intermetallics remained partly intact can be attributed to the relatively higher electrochemical stability of the Mn-containing phase compared with β -AlFeSi, as well as differences in phase interfacial contact and local electrolyte accessibility. Manganese is well established as an effective modifier of Fe-rich intermetallic compounds in primary aluminum alloys. In typical low-iron primary aluminum alloys (0.2 wt%), such as A356 and 6xxx-series alloys, a

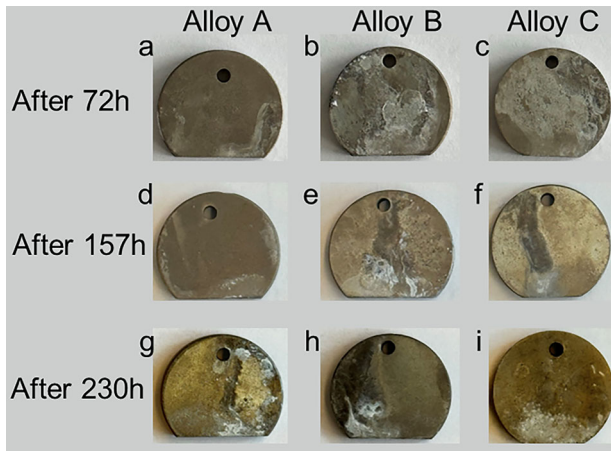
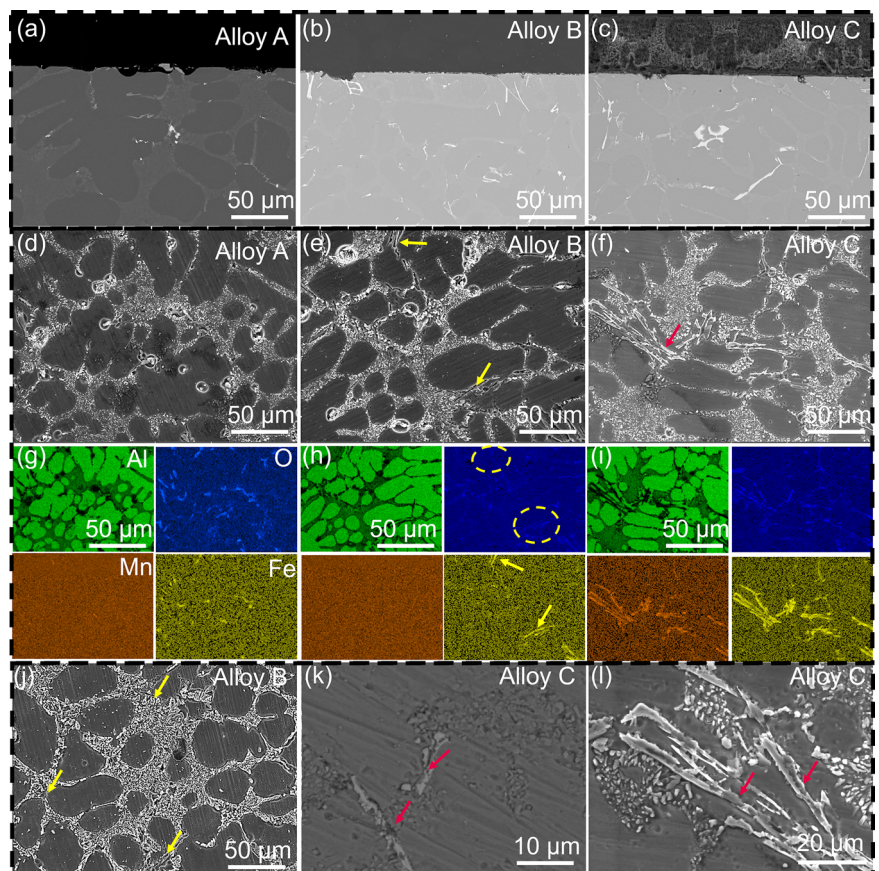


Fig. 5 | Normal surface images of alloys A, B, and C after salt spray. a–c Surface morphologies after 72 hours of salt spray exposure for the three alloys. d–f Morphologies after 157 hours of salt spray exposure for the three alloys. g–i Morphologies after 230 hours of salt spray exposure for the three alloys using a digital camera. Surface roughening and corrosion product accumulation are observed with increasing exposure time for all alloys.

Fig. 6 | SEM images and elemental distribution of alloys A, B, and C under salt spray testing.

a–c Cross-sectional SEM images showing shallow localized penetration, with preferential attack along eutectic Al-Si regions adjacent to the α -Al matrix. d–i Surface morphologies and corresponding EDS spectra. Trenching (yellow arrows) and formation of corrosion products (yellow circles) are observed around β -AlFeSi particles. j–l High-magnification images showing partial dissolution at the periphery of α -Al(FeMn)Si particles, while many intermetallics remain partly intact (red arrows).



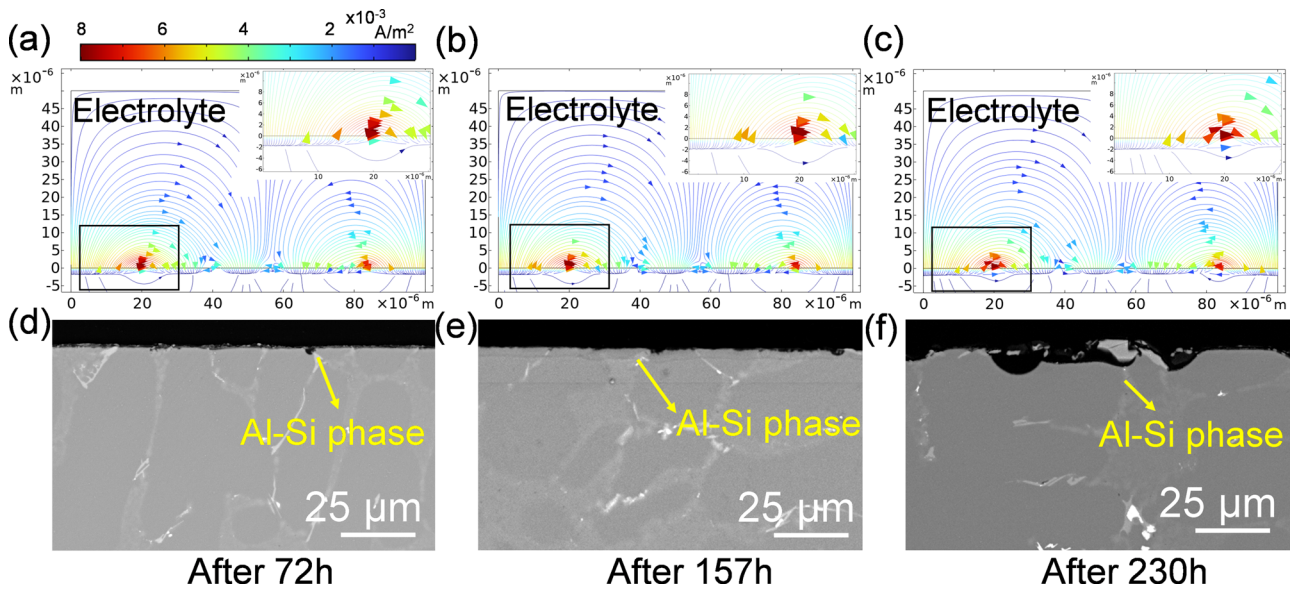


Fig. 7 | Cross-sectional images of the dissolution interface front and electrolyte current density vectors in alloy A after varying exposure times to a 5 wt% NaCl salt spray environment, corresponding to the simulated corrosion process. a–c Finite-element simulations showing electrolyte current density distributions after

72, 157, and 230 hours. Arrows indicate current density vectors, and color contours represent magnitude. The image shows an enlarged view of a selected region. d–f Corresponding experimental cross-sections demonstrating progressive deepening of the corrosion front and localized anodic dissolution of Al-Si phases (yellow arrows).

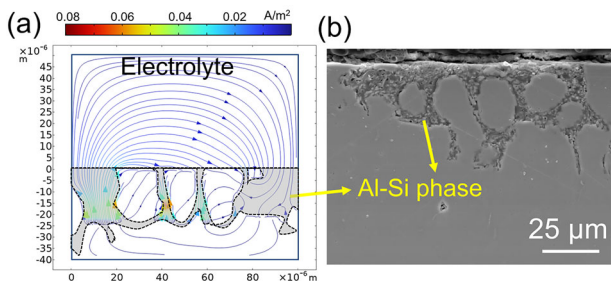


Fig. 8 | Simulated cross-section of corrosion propagation, including electrolyte potential field lines and current densities after virtual 365 days. The final morphology after polarization for alloy A is also shown. a Cross-sectional simulation after a virtual 365 days showing electrolyte potential field lines and current density vectors. Selective dissolution occurs primarily in the eutectic Al-Si phase, whereas the α -Al matrix exhibits negligible current density. b Final corrosion morphology after polarization, displaying characteristic intergranular and localized attack.

Mn/Fe ratio of approximately 0.3 typically partially suppresses the formation of plate-like β -AlFeSi and promotes limited formation of rod-like α -Al(Mn, Fe)Si^{30,39}. However, in alloys containing higher Fe levels (more than 0.5 wt%), substantially higher Mn additions are generally required to achieve a nearly complete transformation of the deleterious β -AlFeSi into Chinese-script α morphologies, with effective Mn/Fe ratios usually approaching or exceeding 1^{29,40,41}. Our concurrent research combined CALPHAD with machine learning to simulate 20 million AlSi7Mg0.3 alloy compositions⁴². This indicates that despite a Mn/Fe ratio greater than 2 being thermodynamically effective in suppressing β -AlFeSi phase formation, excessive manganese addition presents challenges to melt preparation, casting performance, and the mechanical properties of recycled aluminum. In contrast, the Mn/Fe ratio range of 0.25–0.75 promotes efficient α -Al(Mn, Fe)Si phase formation while reducing the total intermetallic phase amount. This narrower range decreases microstructural heterogeneity and influences corrosion susceptibility. Specifically, the α -Al(FeMn)Si phase can promote intergranular corrosion away from innate phases⁴³. Furthermore, it has been reported that a high dislocation density near coarse IMPs may lead to stress concentration, facilitating the formation of defects in the oxide film^{21,23}.

Phase-selected dissolution on the eutectic phase was observed under immersion and polarized conditions in Figs. 3 and 4. In contrast to bulk immersion conditions, salt spray exposure induces distinct electrochemical behavior due to differences in electrolyte morphology and spatial conductivity gradients⁴⁴. In bulk environments, a continuous electrolyte layer enables relatively uniform current distribution. The cathodic reaction is primarily diffusion-controlled oxygen reduction. Contrasting with under salt spray thin film conditions, Oxygen diffuses from the atmosphere across a very short distance between the air-electrolyte interface and the metal surface, readily participating in and accelerating corrosion reactions. The resistance of the electrolyte thus becomes a key parameter controlling the galvanic current. When the electrolyte layer thickness approaches the diffusion layer thickness (approximately 800 μm), a further decrease in film thickness increases electrolyte resistance and consequently decreases the galvanic current⁴⁵. Additionally, the electrolyte resistance is proportional to the electrode distance⁴⁵. As demonstrated by Palani et al.³⁶, the highest anodic current density is highly localized near the cathode edge due to the distribution of geometrical and Ohmic resistance. Under these conditions, stable localized attack and pitting corrosion develop on the exposed surface. The matrix adjacent to Fe-rich phases may experience severe localized activation caused by rapid acidification and chloride accumulation. The resulting damage includes spalling of the β -AlFeSi phase and partial edge corrosion of the α -Al(FeMn)Si phase, as shown in Fig. 6. Therefore, the corrosion mechanism in salt spray differs fundamentally from that in bulk immersion. It is governed by the synergistic effects of thin-film electrolyte geometry, spatial variations in resistance, and the intrinsic electrochemical properties of intermetallic phases. A comparative overview of these corrosion environments is provided elsewhere Table 2.

The micro-galvanic corrosion behavior of contaminated AlSi₇Mg_{0.3} cast alloy was investigated based on electrochemical tests via potentiodynamic polarization and electrochemical impedance spectroscopy, accelerated salt spray test, and numerical simulations. The addition of Fe and Mn refines the size of the α -Al matrix and eutectic Al-Si phases. The cathodic β -AlFeSi phase promotes phase-selective dissolution and trench formation through micro-galvanic corrosion in thin-film electrolyte environments. In contrast, the α -Al(FeMn)Si phase shows lower electrochemical activity and greater morphological stability. Meanwhile, the level-set-based numerical simulations effectively tracked the evolution of the corrosion front in dual-phase microstructures. Although uniform chemical concentration and

Table 2 | Comparison of polarization/impedance tests in bulk electrolyte and salt spray tests under thin-film electrolyte conditions

Feature	Polarization & EIS (Bulk electrolyte)	Salt spray (Thin film)
Electrolyte environment	Quasi-homogeneous bulk immersion	Highly aggressive ⁵³
Corrosion type	Phase-selective dissolution	Localized attack (pitting)
Limiting current density	Constant ($(80 \pm 30) \mu\text{A}/\text{cm}^2$ ¹⁵)	Geometry of thin film electrolyte ⁴⁵
Interface dynamics	Stable interface	Subject to evaporation-condensation cycles
Cathodic kinetics	Diffusion-limited ORR	ORR with reaction control

Table 3 | Composition of three aluminum alloys used in this study (wt%)

Materials	Si	Mg	Fe	Mn	Cu	Al	(Mn/Fe)
Alloy A	6.5–7.5	0.27–0.32	0.12	0.04–0.07	0.05	Bal.	0.3–0.6
Alloy B	6.5–7.5	0.27–0.32	0.55	0.04–0.07	0.05	Bal.	0.07–0.13
Alloy C	6.5–7.5	0.27–0.32	0.55	0.17–0.33	0.05	Bal.	0.3–0.6

neutral pH were assumed, the predicted corrosion morphology and penetration depth were in good agreement with experimental observations. Controlling Mn addition to maintain the Mn/Fe ratio within the range of 0.3–0.6 effectively suppresses the formation of deleterious plate-like β -AlFeSi phases, while promoting the formation of Chinese-script α -Al(FeMn)Si intermetallics. This compositional strategy provides a practical and economically viable approach for the design of secondary aluminum alloys, enhancing their long-term durability in industrial applications, such as lightweight automotive components.

Methods

Materials

Three AlSi7Mg0.3 as-cast alloys with tailored Fe and Mn impurity levels were prepared based on the target compositions for subsequent testing. The chemical compositions of alloys A, B, and C are presented in Table 3. These alloys were cut into coins with a diameter of 20 mm and a thickness of 3 mm.

Electrochemical measurements

Electrochemical impedance spectroscopy (EIS) and potentiodynamic polarization tests were performed on three alloys using a Gamry interface 1000 potentiostat. All measurements were conducted in a naturally aerated 3.5 wt% NaCl solution at room temperature (298 K). Before electrochemical testing, the surface of the specimens was ground with 1200-grit SiC paper and cleaned with ethanol. A conventional three-electrode setup was employed, comprising a Pt wire as the counter electrode, a saturated Ag/AgCl (KCl) reference electrode, and the aluminum specimen as the working electrode with an exposed area of 0.5 cm^2 . Polarization tests were conducted based on the potentiodynamic scanning method. Polarization curves were obtained at a scan rate of 0.5 mV s^{-1} within a potential range of -0.3 V to 1.5 V versus open circuit potential (OCP) after 30 min. EIS measurements were performed over a frequency range of 100 kHz to 0.01 Hz with 10 frequency points per decade after 30 min, using 10 mV RMS sinusoidal perturbation voltage, at predetermined immersion times from 0.5 hours to 12 hours. All measurements were repeated at least three times to ensure reproducibility and reliability. Impedance spectra were analyzed and fitted using ZView software with appropriate equivalent electrical circuits (EECs). Constant phase elements (CPEs) were used in place of ideal capacitors to mathematically account for surface effects and inhomogeneities⁴⁶. The CPE impedance is expressed as:

$$Q = Z_{CPE} = \frac{1}{Y_0(j\omega)^n} \quad (1)$$

where Y_0 is the admittance of CPE, j is the imaginary unit, ω is the angular frequency, and Q and n are the CPE exponents. The exponent n

typically ranges from -1 to 1 , representing pure inductance, resistance, and capacitance, respectively; while the value of n approaching 0.5 is assigned diffusion control, indicating Warburg impedance behavior^{47,48}.

Salt spray test

Salt spray testing was performed in a SC/KWT 450 chamber in general accordance with ASTM B117 standard using a 5 wt% NaCl solution at 35° . Exposure durations were set at 72, 157, and 230 h. After each exposure period, specimens were dried naturally at room temperature for 30 min, then gently rinsed with deionized water to remove soluble salts and dried with an air blower.

Microstructural characterization

After the salt spray test, the surface morphologies were photographically examined using a digital camera. Corrosion products were removed by immersion in a solution of 50 mL H_3PO_4 + 950 mL H_2O at room temperature⁴⁹. Surface and cross-sectional microstructures were analyzed using a scanning electron microscope (SEM, TESCAN Vega 3 SB), equipped with an energy dispersive spectrometer system (EDS, eumeX IXRF systems). Cross-sectional specimens after corrosion were embedded in resin and ground mechanically with 800, 1200, 2500, and 4000-grit SiC papers, and then polished with $1 \mu\text{m}$ colloidal silica suspension. 3D Optical profilometry (VR-5000, Keyence) was utilized to obtain morphology maps of the sample surfaces.

Mathematical modeling and FEM simulations

Finite element method (FEM) simulations were conducted using COMSOL Multiphysics to investigate the micro-galvanic corrosion behavior of Al-Si-Mg cast alloys in a 5 wt% NaCl solution. A two-dimensional model was constructed to represent a simplified microstructure consisting of the primary α -Al matrix and the Al-Si eutectic region. The eutectic region consists of eutectic Al and eutectic Si phases that solidify together within the primary α -Al once the eutectic temperature is reached. Within this region, eutectic Si acts as a local cathode relative to eutectic Al, giving rise to localized micro-galvanic corrosion. Anodic dissolution occurs predominantly within the eutectic region during the early stage of corrosion; this region was considered the main corrosion area in the model.

Figure 9 illustrates a representative cross-sectional microstructure of alloy A, depicting the dendritic α and network-like eutectic Al-Si phases. The model utilizes a level-set method, implemented via an interpolating function to represent the spatial distribution of these phases. The function is defined in Eq. (2), assigning a value of 1 to cathodic regions and 0 to anodic regions. The morphology and distribution of the second phase are based on

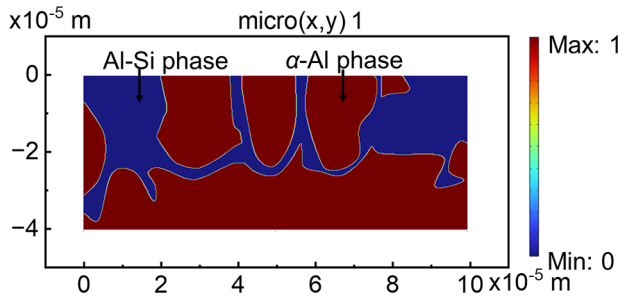


Fig. 9 | A representative cross-sectional microstructure featuring α -Al and Al-Si eutectic phases, modeled using the level-set function defined in Eq. (2). Cross-sectional microstructure of alloy A showing dendritic α -Al and network-like eutectic Al-Si phases. The geometry is implemented using a level-set function to distinguish cathodic and anodic regions for corrosion modeling, where the cathode is defined as 1 and the anode as 0.

alloy A.

$$\text{micro}(x, y) = \begin{cases} 1, & \text{cathode} \\ 0, & \text{anode} \end{cases} \quad (2)$$

The electrolyte potential field is governed by Ohm's law, assuming a well-mixed and static electrolyte with negligible concentration gradients for simplicity. The relation between the electrolyte current density i_l and the electric potential ϕ_l is given by Eq. (3)⁵⁰:

$$i_l = -\sigma_l \nabla \phi_l \quad (3)$$

where σ_l is the constant (7.8S/m)³ electrical conductivity of the test electrolyte. Charge conservation within the domain requires the sum of currents to be zero:

$$\nabla \cdot i_l = 0 \quad (4)$$

This implies no accumulation of charge within the electrolyte domain. For all boundaries not in contact with electrodes, an insulation boundary condition is applied:

$$n \cdot i_l = 0 \quad (5)$$

where n is the normal vector pointing outward from the domain. These assumptions simplify the electrochemical transport model to a quasi-static, purely electrically driven system.

Electrochemical reactions are confined to electrode surfaces. The cathodic reaction here corresponds to oxygen reduction:



Anodic reaction represents classical aluminum dissolution:



The α -Al phase functions as a cathodic site in the micro-galvanic couple and does not participate in anodic dissolution. The reaction kinetics at both anodic and cathodic sites are defined in the first approximation by polarization curves. Electrochemical kinetics parameters were modeled using the polarization curves obtained from Wu et al.⁵¹ for eutectic Al-Si-Mg alloys and from Asrari et al.⁵² for pure Al, as shown in Fig. 10. The boundary conditions integrate local current density with electrolyte potential through an interpolation function of polarization data $\phi_{cathode}$ and ϕ_{anode}

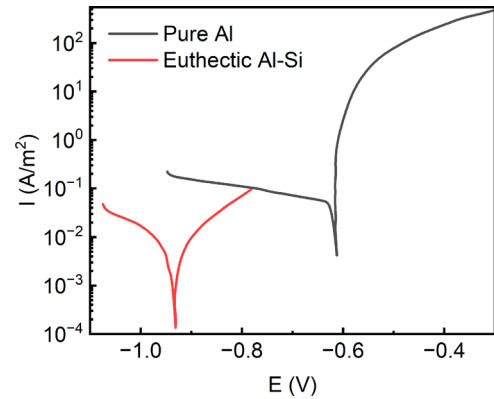


Fig. 10 | Potentiodynamic polarization curves for eutectic Al-Si alloy and pure Al in 3.5 wt% NaCl solution, adopted from^{51,54}. Potentiodynamic polarization curves reproduced from previous studies and used as electrochemical kinetic inputs for the simulations. Data were adapted from Wu et al. and Jahan et al.

respectively:

$$i_{cathode} = f(\phi_{cathode} - \phi_l) \times \text{micro}(x, y) \quad (8)$$

$$i_{anode} = f(\phi_{anode} - \phi_l) \times (1 - \text{micro}(x, y)) \quad (9)$$

The normal dissolution rate (interface velocity) of the anodic dissolution front R_c is calculated using Faraday's law as:

$$R_c = \frac{i_{loc} M_{Al}}{zF\rho_{Eutectic}} \times (1 - \text{micro}(x, y)) \quad (10)$$

where M_{Al} is the average molar mass 26.98 g mol⁻¹ of Al, ρ is the density (2700 kg m³) of the eutectic phase. i_{loc} is the local current density of the electrode surface. z is the charge number of Al, F is the Faraday constant.

The evolution of the moving corrosion front is tracked using the level-set method, with the governing equation given by:

$$\frac{\partial \phi}{\partial t} + R_c \nabla \phi = \gamma \nabla \cdot \left(\varepsilon \nabla \phi - \phi(1 - \phi) \frac{\partial \phi}{|\nabla \phi|} \right) \quad (11)$$

Here, the parameter ε is the interface thickness parameter, defined as $\varepsilon = h_{max}/8$, where h_{max} is the maximum mesh cell size in the domain. The reinitialization parameter γ is set to the maximum dissolution rate in the system. ϕ is the level-set function ranging from 1 (electrode) to 0 (electrolyte).

Data availability

The datasets generated and/or analyzed during the current study are not publicly available due to [the data are part of an ongoing study and contain intellectual property that is subject to confidentiality] but are available from the corresponding author on reasonable request.

Received: 17 November 2025; Accepted: 2 March 2026;

Published online: 20 March 2026

References

- Li, S.-S. et al. Development and applications of aluminum alloys for aerospace industry. *J. Mater. Res. Technol.* **27**, 944–983 (2023).
- You, X. et al. A review of research on aluminum alloy materials in structural engineering. *Dev. Built Environ.* **17**, 100319 (2024).
- Kadowaki, M., Katayama, H. & Yamamoto, M. Galvanic current analysis of AA6016/SM490 couple using experimental and numerical

- simulation data in various NaCl solutions. *Corros. Sci.* **211**, 110918 (2023).
4. Singh, P., Ramacharyulu, D. A., Kumar, N., Saxena, K. K. & Eldin, S. M. Change in the structure and mechanical properties of Al-Mg-Si alloys caused by the addition of other elements: A comprehensive review. *J. Mater. Res. Technol.* **27**, 1764–1796 (2023).
 5. Arthanari, S., Jang, J. C. & Shin, K. S. Corrosion performance of high pressure die-cast Al-Si-Mg-Zn alloys in 3.5 wt% NaCl solution. *J. Alloy. Compd.* **783**, 494–502 (2019).
 6. Šurđová, Z. et al. The influence of Fe content on corrosion resistance of secondary AlSi7Mg0.3 cast alloy with increased Fe-content. *Manuf. Technol.* **22**, 598–604 (2022).
 7. Ji, Y. et al. Review of micro-scale and atomic-scale corrosion mechanisms of second phases in aluminum alloys. *Trans. Nonferrous Met. Soc. China* **31**, 3205–3227 (2021).
 8. Al-Alimi, S. et al. Recycling aluminium for sustainable development: A review of different processing technologies in green manufacturing. *Results Eng.* **23**, 102566 (2024).
 9. Raabe, D. et al. Making sustainable aluminum by recycling scrap: The science of “dirty” alloys. *Prog. Mater. Sci.* **128**, 100947 (2022).
 10. Zhou, B. et al. Microstructure evolution of recycled 7075 aluminum alloy and its mechanical and corrosion properties. *J. Alloys Compd.* **879**, 160407 (2021).
 11. Borgert, T. & Homberg, W. Energy saving potentials of an efficient recycling process of different aluminum rejects. *Energy Rep.* **8**, 399–404 (2022).
 12. Wang, T. et al. Upcycled high-strength aluminum alloys from scrap through solid-phase alloying. *Nat. Commun.* **15**, 1–8 (2024).
 13. Vargel, C. *Corrosion of aluminium* (Elsevier, Boston, 2020).
 14. Arrabal, R. et al. Pitting corrosion of rheocast A356 aluminium alloy in 3.5 wt.% NaCl solution. *Corros. Sci.* **73**, 342–355 (2013).
 15. Adapala, P. et al. Understanding the effect of microstructure and composition on localized corrosion susceptibility of 6xxx aluminum alloys. *npj Mater. Degrad.* **8**, 52 (2024).
 16. Tian, H. et al. Atmospheric corrosion and mechanical property degradation of 2524-T3 aluminum alloy in marine environments. *Corros. Sci.* **239**, 112398 (2024).
 17. Zhang, X. et al. Morphology, thermal stability, electronic structure and mechanical properties of α -AlFeMnSi phases with varying Mn/Fe atomic ratios: Experimental studies and DFT calculations. *J. Alloy. Compd.* **901**, 163523 (2022).
 18. Kim, J., Shin, S. & Lee, S. Correlation between microstructural evolution and corrosion resistance of hypoeutectic Al-Si-Mg alloy: Influence of corrosion product layer. *Mater. Charact.* **193**, 112276 (2022).
 19. Reboul, M. C. & Baroux, B. Metallurgical aspects of corrosion resistance of aluminium alloys. *Mater. Corros.* **62**, 215–233 (2010).
 20. Mingo, B., Arrabal, R., Pardo, A., Matykina, E. & Skeldon, P. 3D study of intermetallics and their effect on the corrosion morphology of rheocast aluminium alloy. *Mater. Charact.* **112**, 122–128 (2016).
 21. Kayani, S. H., Ha, H.-Y., Cho, Y.-H., Son, H.-W. & Lee, J.-M. Dislocation-assisted localised pitting corrosion behaviour of Al-Si-Mg-Cu-Mn alloy. *Corros. Sci.* **221**, 111372 (2023).
 22. Kayani, S. H. et al. Impact of intermetallic phases on the localised pitting corrosion and high-temperature tensile strength of Al-Si-Mg-Cu-Ni alloys. *Corros. Sci.* **233**, 112064 (2024).
 23. Gao, Y. et al. Distinctive localized corrosion behavior of β -Mg₂Si and α -Al(Fe, Mn)Si phases in a 6082 alloy. *J. Mater. Res. Technol.* **29**, 1675–1682 (2024).
 24. Kuijpers, N. et al. The dependence of the β -al-fesi to α -Al(FeMn)Si transformation kinetics in Al-Mg-Si alloys on the alloying elements. *Mater. Sci. Eng. A* **394**, 9–19 (2005).
 25. Kuijpers, N., Vermolen, F., Vуйk, C. & van der Zwaag, S. A model of the β -AlFeSi to α -Al(FeMn)Si transformation in Al-Mg-Si alloys. *Mater. Trans.* **44**, 1448–1456 (2003).
 26. Chen, X.-M. et al. Fe-bearing intermetallics transformation and its influence on the corrosion resistance of Al-Mg-Si alloy weld joints. *J. Mater. Res. Technol.* **9**, 16116–16125 (2020).
 27. Verma, A., Kumar, S., Grant, P. & O'Reilly, K. Influence of cooling rate on the Fe intermetallic formation in an AA6063 Al alloy. *J. Alloy. Compd.* **555**, 274–282 (2013).
 28. Lan, X. et al. Preparation of millimeter-scale second-phase particles in aluminum alloys and determination of their mechanical properties. *J. Alloy. Compd.* **784**, 68–75 (2019).
 29. Hwang, J., Doty, H. & Kaufman, M. The effects of Mn additions on the microstructure and mechanical properties of Al-Si-Cu casting alloys. *Mater. Sci. Eng. A* **488**, 496–504 (2008).
 30. Kim, H. Y., Park, T. Y., Han, S. W. & Lee, H. M. Effects of Mn on the crystal structure of α -Al(Mn,Fe)Si particles in A356 alloys. *J. Cryst. Growth* **291**, 207–211 (2006).
 31. Kim, B., Lee, S., Lee, S. & Yasuda, H. Real-time radiographic observation of solidification behavior of Al-Si-Cu casting alloys with the variation of iron content. *Mater. Trans.* **53**, 374–379 (2012).
 32. Peng, Y. et al. Galvanic corrosion between Al-Zn-Mg-Cu alloy and stainless steel in the salt-spray atmosphere. *Mater. Chem. Phys.* **294**, 127009 (2023).
 33. Abodi, L. C. et al. Simulated and measured response of oxygen SECM-measurements in the presence of a corrosion process. *Electrochim. Acta* **146**, 556–563 (2014).
 34. Ji, S., Yang, W., Gao, F., Watson, D. & Fan, Z. Effect of iron on the microstructure and mechanical property of Al-Mg-Si-Mn and Al-Mg-Si diecast alloys. *Mater. Sci. Eng. A* **564**, 130–139 (2013).
 35. Kuchariková, L. et al. Analysis of microstructure in AlSi7Mg0.3 cast alloy with different content of Fe. *Transp. Res. Procedia* **40**, 59–67 (2019).
 36. Palani, S., Hack, T., Deconinck, J. & Lohner, H. Validation of predictive model for galvanic corrosion under thin electrolyte layers: An application to aluminium 2024-CFRP material combination. *Corros. Sci.* **78**, 89–100 (2014).
 37. Wang, M. et al. Study on the roles of bisulfite in the stress corrosion cracking of 7050-T7451 aluminum alloy in the thin electrolyte layer environment. *Corros. Sci.* **215**, 111030 (2023).
 38. Cao, X. & Hu, X. The investigation of micro-galvanic corrosion of SAF 2205 duplex stainless steel based on numerical simulation model and immersion test. *Corros. Sci.* **207**, 110601 (2022).
 39. Xu, Z. et al. Effect of Mn/Fe ratio on the microstructure and properties of 6061 sheets obtained by twin-roll cast. *Mater. Charact.* **168**, 110536 (2020).
 40. Song, D. et al. Effect of Mn/Fe ratio on Fe removal efficiency and tensile ductility of an Al-_{7.0}Si-_{2.4}Fe alloy. *J. Mater. Res.* **36**, 1357–1366 (2021).
 41. Gao, T., Hu, K., Wang, L., Zhang, B. & Liu, X. Morphological evolution and strengthening behavior of α -Al(FeMn)Si in Al-6Si-2Fe-xMn alloys. *Results Phys.* **7**, 1051–1054 (2017).
 42. Jaren, L. C. et al. Machine learning-accelerated CALPHAD analysis of impurity-driven intermetallic formation in secondary AlSi₇Mg_{0.3}. *npj Mater. Sustain.* <https://doi.org/10.1038/s44296-026-00097-9> (2026). In press.
 43. Bartawi, E. et al. The effect of trace level copper content on intergranular corrosion of extruded AA6082-T6 alloys. *Mater. Chem. Phys.* **309**, 128303 (2023).
 44. Liu, C., Kubacki, G. W. & Kelly, R. G. Application of laplace equation-based modeling into corrosion damage prediction for galvanic coupling between a zinc plate and stainless steel rods under a thin film electrolyte. *Corrosion* **75**, 465–473 (2019).
 45. Liu, C., Srinivasan, J. & Kelly, R. G. Editors' choice—electrolyte film thickness effects on the cathodic current availability in a galvanic couple. *J. Electrochem. Soc.* **164**, C845 (2017).
 46. Nahir, T. M. *Impedance Spectroscopy: Theory, Experiment, and Applications* (ACS Publications, New Jersey, 2005).

47. Wang, B. et al. Investigation on the corrosion behavior of aluminum alloys 3A21 and 7A09 in chloride aqueous solution. *Mater. Des* **50**, 15–21 (2013).
48. Rahimi, E. et al. Atmospheric corrosion of iron under a single droplet: A new systematic multi-electrochemical approach. *Corros. Sci.* **235**, 112171 (2024).
49. Blawert, C. et al. Effects of mechanical surface pre-treatment on integrity and corrosion of bare and coated AA6082 substrates. *J. Mater. Res. Technol.* **31**, 844–859 (2024).
50. Deshpande, K. B. Numerical modeling of micro-galvanic corrosion. *Electrochim. Acta* **56**, 1737–1745 (2011).
51. Wu, Y. & Liao, H. Corrosion behavior of extruded near eutectic Al-Si-Mg and 6063 alloys. *J. Mater. Sci. Technol.* **29**, 380–386 (2013).
52. Asrari, G., Daneshifar, M., Hosseini, S. & Alishahi, M. Selective alloying of pure aluminum with varying amounts of magnesium using friction stir processing for improved mechanical and corrosion-resistant properties. *Mater. Chem. Phys.* **306**, 128091 (2023).
53. Chinara, M., Ghosh, R., Mukherjee, S. & Mondal, K. Corrosion mechanism of line pipe steels (API X70 and X80 grades) under aggressive salt-spray exposure. *Mater. Chem. Phys.* **339**, 130762 (2025).
54. Jahan, A., Alam, M. A., Suzuki, E. & Yashiro, H. Corrosion behavior of pure aluminum in the simulated and real environments for use as a bipolar plate component in polymer electrolyte membrane fuel cells. *Ind. Eng. Chem. Res.* **62**, 20223–20235 (2023).

Acknowledgements

The authors would like to thank Dr. D. Snihirova for valuable scientific discussions. Technical assistance from Mr. U. Burmester and Mr. V. Heitmann is also gratefully acknowledged. Qiqi Li was supported by the China Scholarship Council under fellowship Grant no. 202308500042. Eugen Gazenbiller, Lukas Cäsar Jarren and Daniel Höche thank the Bundesministerium für Wirtschaft und Energie (Grant number 03LB3091A-F) for the financial support.

Author contributions

Qiqi Li: Conceptualization, Methodology, Investigation, Data curation, Writing – original draft, Writing – review & editing. Eugen Gazenbiller: Conceptualization, Methodology, Writing – review & editing. Lukas Cäsar

Jarren: Conceptualization. Mikhail L. Zheludkevich: Writing – review & editing. Daniel Höche: Conceptualization, Writing – review & editing. All authors have read and approved the manuscript.

Funding

Open Access funding enabled and organized by Projekt DEAL.

Competing interests

The authors declare that they have no known competing financial interests or personal relationships that could have appeared to influence the work reported in this paper. Author Mikhail L. Zheludkevich is Associate Editor of npj materials degradation. Mikhail L. Zheludkevich was not involved in the journal's review of, or decisions related to, this manuscript.

Additional information

Correspondence and requests for materials should be addressed to Qiqi Li.

Reprints and permissions information is available at <http://www.nature.com/reprints>

Publisher's note Springer Nature remains neutral with regard to jurisdictional claims in published maps and institutional affiliations.

Open Access This article is licensed under a Creative Commons Attribution 4.0 International License, which permits use, sharing, adaptation, distribution and reproduction in any medium or format, as long as you give appropriate credit to the original author(s) and the source, provide a link to the Creative Commons licence, and indicate if changes were made. The images or other third party material in this article are included in the article's Creative Commons licence, unless indicated otherwise in a credit line to the material. If material is not included in the article's Creative Commons licence and your intended use is not permitted by statutory regulation or exceeds the permitted use, you will need to obtain permission directly from the copyright holder. To view a copy of this licence, visit <http://creativecommons.org/licenses/by/4.0/>.

© The Author(s) 2026